Journal of Materials Chemistry A

ROYAL SOCIETY OF CHEMISTRY

COMMUNICATION

View Article Online
View Journal | View Issue

Cite this: J. Mater. Chem. A, 2022, 10, 19641

Received 21st March 2022
Accepted 24th May 2022

DOI: 10.1039/d2ta02229j

rsc.li/materials-a

In situ construction of polyether-based composite electrolyte with bi-phase ion conductivity and stable electrolyte/electrode interphase for solid-state lithium metal batteries†

Shujun Zheng,[a] Yuyang Chen,[a] Kai Chen,[a] Shengyuan Yang,[a] Roohollah Bagherzadeh,[c] Yue-E Miao *[a] and Tianxi Liu[ab]

Polyether-based composite electrolytes exhibit great promise to bridge the gap between solid polymer electrolytes (SPEs) and high-energy solid-state Li metal batteries. However, the practical application of polyether electrolytes is still hindered by their poor ionic conductivity and low oxidation potential. Herein, a topochemistry-driven polyether-based composite electrolyte is constructed *in situ*, by the cation polymerization of 1,3-dioxolane (DOL) to obtain poly(1,3-dioxolane) (PDOL) in a three-dimensional (3D) $La_{0.56}Li_{0.33}TiO_3$ nanofiber (LLTO NF) skeleton, with a chemically stable interface and strong-coupled ionic conductivity. The spontaneous polymerization reaction results in the formation of a unique polymeric CH_2–CH_2–O–CH_2–O– amorphous structure of PDOL, with a wide operation voltage (5.5 V) and an intimate interface within the LLTO NF skeleton. The continuous one-dimensional (1D) LLTO NFs and polymer chains act as bi-phase ion transport channels, enabling an improved conduction of 6.6×10^{-4} S cm^{-1}. Furthermore, the LiF and Al-complex films derived from the solid electrolyte interphase (SEI) can redistribute the ion flux and ensure the structural stability of the Li anode. Thus, the polyether-based composite electrolyte achieves a remarkable cyclability (over 900 h at 0.1 mA cm^{-2}) and satisfactory capacity retention (70.7% over 350 cycles). This polymer composite electrolyte design offers a unique perspective for linking *in situ* topochemistry design with safe and high-energy solid batteries.

Introduction

Triggered by the increasing demand for technologies ranging from flexible electronics and electric vehicles to electrical grids,[1–3] there is an urgent need for a breakthrough in electrochemical energy storage systems. The lithium (Li) metal anode is a very promising candidate for high-energy lithium metal batteries (LMBs), due to its high specific capacity (3860 mA h g^{-1}) and ultra-low redox potential (−3.04 V *vs.*

[a]State Key Laboratory for Modification of Chemical Fibers and Polymer Materials, College of Materials Science and Engineering, Donghua University, Shanghai, 201620, China. E-mail: yuee_miao@dhu.edu.cn

[b]Key Laboratory of Synthetic and Biological Colloids, Ministry of Education, School of Chemical and Material Engineering, Jiangnan University, Wuxi, 214122, China

[c]Advanced Fibrous Materials LAB, Institute for Advanced Textile Materials and Technologies (ATMT), School of Advanced Materials and Processes, Amirkabir University of Technology, Tehran, Iran

† Electronic supplementary information (ESI) available. See https://doi.org/10.1039/d2ta02229j

Dr Yue-E Miao received her BS degree from Southeast University in 2010 and PhD degree from Fudan University in 2015. In 2013, she was a joint-training graduate student in the School of Physical & Mathematical Sciences at Nanyang Technological University, Singapore. She is now an associate professor in College of Materials Science and Engineering, Donghua University. She serves as a Young Editorial Board Member for the journal Exploration. Her research interests mainly focus on the design and synthesis of polymer nanofiber composites, including polymer nanofiber electrolytes/separators, organic nanofiber electrodes, carbon nanofiber composites, for applications in electrochemical energy storage (such as Li/Na-ion batteries and Li–S batteries).

standard hydrogen electrode).[4–6] However, it suffers from uncontrollable dendritic growth, electrolyte corrosion, and thermodynamic instability in liquid LMBs.[7,8] Developing solid-state electrolytes (SSEs) can overcome the above hindrances while also achieving improved security.

Among existing SSEs, solid polymer electrolytes (SPEs) stand out for their superior flexibility, designability and intimate interfacial contact.[9–11] However, the traditional polyethylene oxide (PEO) electrolyte, one of the main commercial electrolytes, faces many obstacles, including insufficient ionic conduction (10^{-6} to 10^{-8} S cm^{-1}, at room temperature) and a low oxidation potential (3.8 V *vs.* Li/Li^+).[12–14] Composite polymer electrolytes (CPEs) can bridge the above gaps by integrating active inorganic fillers into polyether electrolytes.[15–17] The rigid inorganic fillers in CPEs, with their inherent high ion conductivity, play a critical role in suppressing the agglomeration of polymer chains and accelerating the dissociation of Li salt.[18,19] Moreover, flexible macromolecular chains are effective for optimizing the electrode–electrolyte interface, providing efficient intermolecular/intramolecular Li-ion migration.[20–22] Nevertheless, it is still a great challenge to selectively design flexible-rigid integrated CPEs to realize superior conductivity and interface compatibility simultaneously for maximized long-term cyclability of solid metal batteries.

Herein, we propose a rational topochemistry-driven polymerization tactic for the construction of a bi-phase ion conductive polyether-based composite electrolyte with a chemically stable interphase. The composite electrolyte is prepared by the cationic polymerization of 1,3-dioxolane (DOL) to obtain poly(1,3-dioxolane) (PDOL) in a self-supporting $La_{0.56}Li_{0.33}TiO_3$ nanofiber (LLTO NF) framework, which is denoted as *In-situ* PLE. The topochemistry design endows the polyether-based composite electrolyte with remarkable merits: (i) the unique amorphous structure of the CH_2–CH_2–O–CH_2–O– chain in PDOL obtained by *in situ* polymerization ensures intimate electrode/electrolyte interfacial contact, which allows for fast bulk/interfacial transfers and a broadened voltage window; (ii) the rich LiF and Al-complex solid electrolyte interphase (SEI) can serve as an ionic rectifier layer to redistribute ion flux, thereby reducing the accumulation of dead Li and inhibiting dendritic growth; (iii) the 1D–1D interconnected interface between PDOL polymer chains and LLTO NFs can offer highly efficient bi-phase transport pathways. Therefore, the *In-situ* PLE achieves a dense, dendrite-free Li circulating layer over 900 h and a largely improved long-term cyclability of 70.7% over 350 cycles at 0.5C.

Results and discussion

The composite polyether electrolyte containing PDOL and LLTO NFs is denoted as PLE. Under an *in situ* polymerization condition of DOL, as illustrated in Fig. 1a, the as-prepared sample is the *In-situ* PLE. For comparison, PLE obtained under an *ex situ* polymerization of DOL is denoted as *Ex-situ* PLE, while the PDOL electrolyte without LLTO NFs is also prepared *via in situ* polymerization as a control sample. Typically, LiTFSI is added to all electrolytes, but they are ignored in the naming. First, the self-supporting LLTO NF skeleton was obtained by a simple electrospinning-sintering method.[23] Fig. 1b and S1a† shows continuous porous LLTO nanofibers with a diameter of ~500 nm, derived from the flexible precursor nanofiber membrane with a uniform fiber diameter of 570 nm and concentrated pore size of 1.48 μm (Fig. S2†), forming a three-dimensional (3D) skeleton structure. A high specific surface area of 35.685 $m^2 g^{-1}$ with a mesoporous pore size of 15.84 nm is obtained for the LLTO NFs (Fig. S3†). The inset in Fig. 1b confirms the homogenous distribution of La, Ti, and O elements. These results suggest that the interconnected and porous structure of the ceramic LLTO electrolyte is advantageous for continuous ion conduction. In addition, a clear lattice spacing of 2.7 Å corresponding to the (110) plane of the LLTO crystal can be observed in Fig. S1b and S1c,† [24] confirming its high crystallinity and that the fastest ion transfer occurs along the [001] direction.[25]

Subsequently, the DOL solution was allowed to permeate into the LLTO skeleton, and the cation ring-opening polymerization was completed within 12 h.[26,27] To construct a thin ion-conductive skeleton, the thickness of the LLTO NF matrix was controlled to be 150 μm. As shown in Fig. 1c, a smooth and flat solid structure is acquired after introducing the pre-polymerized precursor into the LLTO NF matrix. The final thickness of the *In-situ* PLE remains at 144 μm, as shown in the typical cross-sectional scanning electron microscope (SEM) image (Fig. S4†). It is clear that the LLTO NFs are completely covered by PDOL without obvious pores in Fig. 1d, demonstrating that the precursor solution is uniformly filled into the porous LLTO NF matrix and gradually forms a polymer network. This suggests the formation of a dense bi-phase ion conduction network, where the LLTO NF skeleton acts as a 3D continuous Li-ion transport channel. Meanwhile, the PDOL phase permeated in LLTO can achieve rapid ion conduction through the coupling/decoupling of O and Li^+ in the –CH_2–CH_2–O–CH_2–O– polymer chains.[13,28]

To further analyze the topochemistry of PDOL, nuclear magnetic resonance (NMR) measurements were performed (Fig. 1e). Obviously, the pristine liquid DOL electrolyte was transformed into a transparent solid polyether electrolyte after adding a small dose of $Al(OTf)_3$. Al^{3+} attacked the oxygen atoms in DOL, causing the ring-opening polymerization,[29] while two new signals at 3.61 ppm and 4.64 ppm are ascribed to proton peaks from the –O–CH_2–CH_2– and –O–CH_2–O– groups, respectively, which agrees well with the repeating unit of –CH_2–CH_2–O–CH_2–O– in PDOL.[27] It is worth mentioning that the bare DOL electrolyte without Lewis-acid additives shows no obvious change. Then, Fourier transform infrared spectroscopy (FTIR) was conducted to discern the changes in the molecular structure during the polymerization process of the *In-situ* PLE (Fig. 1f). After curing for 12 h, the out-of-plane C–H vibration peak disappears, and the peak position of C–O–C shifts from 1030 cm^{-1} to 1000 cm^{-1}, along with the appearance of a long-chain structure belonging to PDOL.[26] The conspicuous changes of these characteristic peaks confirm the successful polymerization of PDOL. In addition, the FTIR spectrum of PDOL obtained from the *In-situ* PLE is consistent with that of

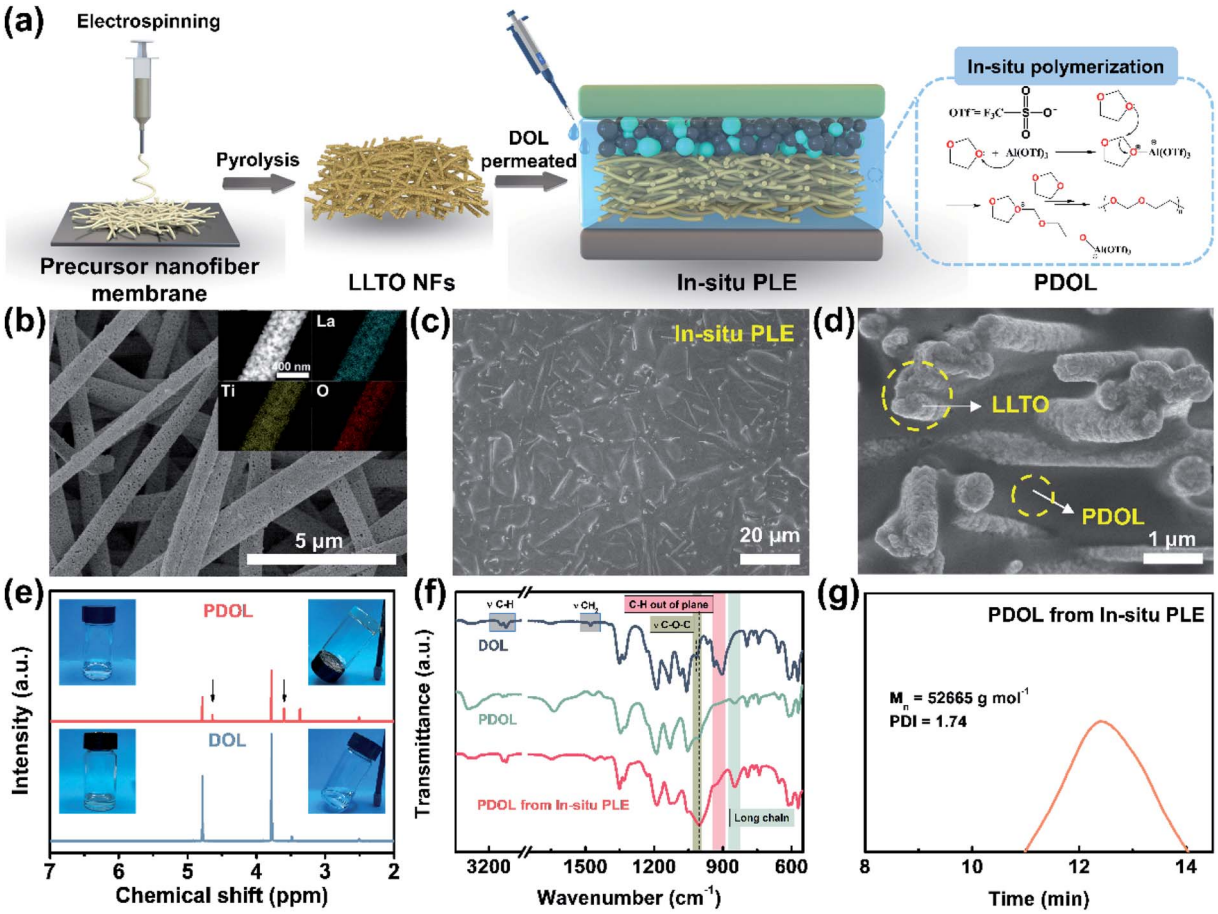

Fig. 1 (a) Schematic illustrating the preparation of the *In-situ* PLE *via in situ* polymerization. (b) Surface morphology of LLTO NFs membrane. The inset shows the EDS mappings of La, Ti, and O elements. SEM images of the *In-situ* PLE: (c) surface, and (d) cross-section. (e) ^{1}H NMR spectra of liquid DOL and solid PDOL. The inset depicts the unchanged liquid DOL electrolyte and solidified PDOL electrolyte. (f) FTIR spectra. (g) The average molecular weight of PDOL obtained by GPC.

pure PDOL, indicating that the cationic polymerization process of DOL is not affected by the LLTO NFs. Furthermore, the final molecular weight of PDOL was measured to be 52 665 g mol^{-1} from the gel permeation chromatography (GPC) result (Fig. 1g).

The physicochemical and electrochemical properties of the *In-situ* PLE were then systematically examined. As shown in Fig. 2a, the liquid DOL begins to volatilize at 30 °C, whereas the PDOL electrolyte shows a significantly improved thermal stability with a decomposition temperature up to 100 °C. The weight loss of all the electrolytes at about 400 °C is due to the thermolysis of LiTFSI.[26] No mass loss is observed throughout the pyrolysis process of LLTO NFs, indicating its excellent thermal stability.[30] Direct evidence can also be provided by the combustion experiments shown in Fig. 2b and c. A fast and short burn-out process is observed for the PDOL electrolyte with a duration of 8 s (Video S1†), which can be ascribed to the remaining DOL solvent and the low melting point of PDOL. Surprisingly, the *In-situ* PLE, in combination with the highly flame-retardant LLTO NF matrix, displays satisfactory self-extinguishing characteristics and maintains structural integrity, even if it burns within the first few seconds (Video S2†). This is in contrast to the severe thermal melting presented in a commercial Celgard separator (Fig. S5 and video S3†).

Apart from the good flame retardancy, the *In-situ* PLE also exhibits excellent electrochemical properties. Although the PEO electrolyte is stable in combination with the Li anode, the narrow window of only 4.1 V limits its practical applications. With the novel polyether of PDOL obtained by an *in situ* topochemistry design, the electrochemical window of the *In-situ* PLE can be expanded to 5.5 V (Fig. 2d), which is suitable for almost all commercial cathode materials. Importantly, an ion migration number of 0.6 can be reached (Fig. 2e and S6†), which significantly exceeds that of the traditional PEO electrolyte (t_{Li^+} = 0.2).[13,31] This can be attributed to the fact that the continuous functional –C–O– groups in the PDOL network can provide unique ion coordination for Li^+ and accelerate ion migration. Considering that the conductivity of SPE is in connection with its amorphous state and the free volume from rubber to viscoelastic state above the glass transition temperature (T_g), differential scanning calorimeter (DSC) tests were carried out to study the thermal behavior of PDOL. Fig. S7† shows the crystalline structure for the salt-free PDOL, in which a large melting peak (T_m) and recrystallization peak can be observed, while the

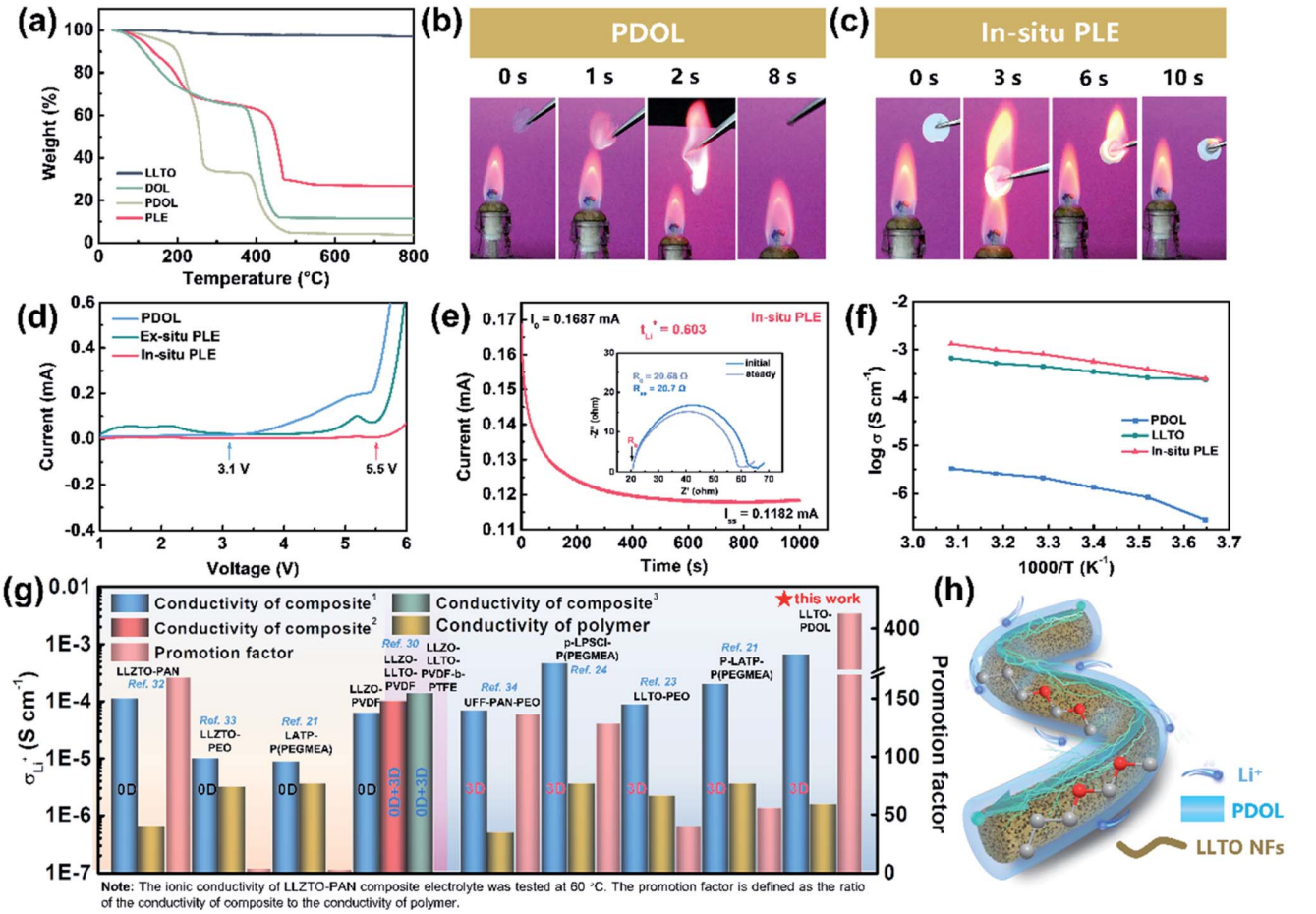

Fig. 2 Physicochemical properties of DOL and different electrolytes. (a) TGA curve. Combustion tests of (b) PDOL and (c) PLE electrolytes. (d) LSV curve, and (e) current–time profile of the Li|*In-situ* PLE|Li symmetrical cell after applying a DC voltage of 10 mV. (f) Ionic conductivity under different temperatures. (g) Comparisons of the ionic conductivity with different solid electrolytes. (h) Schematic diagram of the bi-phase ion conduction within the *In-situ* PLE.

PDOL-LiTFSI electrolyte presents an amorphous state with only a T_g point due to the plasticizing effect.[29] Further evidence can be estimated by the activation energy (E_a) of Li^+ migration in Fig. 2f. The value (0.165 eV) for the *In-situ* PLE is much lower than those of the PDOL (0.363 eV) and LLTO electrolytes (0.255 eV). Moreover, the room-temperature Li^+ conductivity obtained in this work is 6.6×10^{-4} S cm^{-1}, which is much higher than those of most previous studies (Fig. 2g).[21,23,24,30,32–34] This can be attributed to the inherent amorphous structure and low T_g point of PDOL, as well as the continuous 3D Li^+ transfer channels in LLTO NFs (Fig. 2h). Taken together, the superior self-extinguishing, wide voltage windows, and rapid bi-phase ion conductive paths not only make up for the two major shortcomings of traditional polyether electrolytes, but also suggest great potential for solid batteries with long-term cyclability.

In situ polymerization is deemed as the most universal solution to improve interfacial compatibility. As shown in Fig. 3a, three types of electrolytes were extended into symmetric cells to evaluate the voltage polarization phenomenon and long-term cycling stability. The Li|*Ex-situ* PLE|Li cell shows a sharply increased polarization voltage over 2 V in just a few minutes, together with a heavier voltage fluctuation and battery failure (inset in Fig. 3a) at a constant current density of 0.1 mA cm^{-2}. Meanwhile, the cell with the PDOL electrolyte displays a smaller overpotential than that of the *Ex-situ* PLE-based symmetric cell, which undergoes continuous and unstable fluctuations and causes a short circuit at 100 h. In contrast, the Li|*In-situ* PLE|Li cell displays superior cycling stability for over 900 h with a stable overpotential of ~40 mV. The enlarged voltage profiles after different times also show no significant polarization for the *In-situ* PLE prepared *via in situ* polymerization (Fig. 3a$_1$–a$_3$). The current density further improved to 0.5 mA cm^{-2}, and the *In-situ* PLE remains stable at about 280 mV for 400 h (Fig. S8†). We determined that the excellent long-term interfacial stability derived from the high ionic conductivity of the *In-situ* PLE and the *in situ* improved electrode–electrolyte interfacial compatibility. The interfacial stability of the Li|*In-situ* PLE|Li cell was further substantiated by electrochemical impedance spectra (EIS) tests (Fig. 3b, S9 and S10†). Obviously, the interfacial impedance (R_{ct}) of the Li|*Ex-situ* PLE|Li cell is about 4957 Ω, which is 100 times than that (40.37 Ω) of the Li|PDOL|Li cell. We can infer that the extremely high R_{ct} of the *Ex-situ* PLE derived

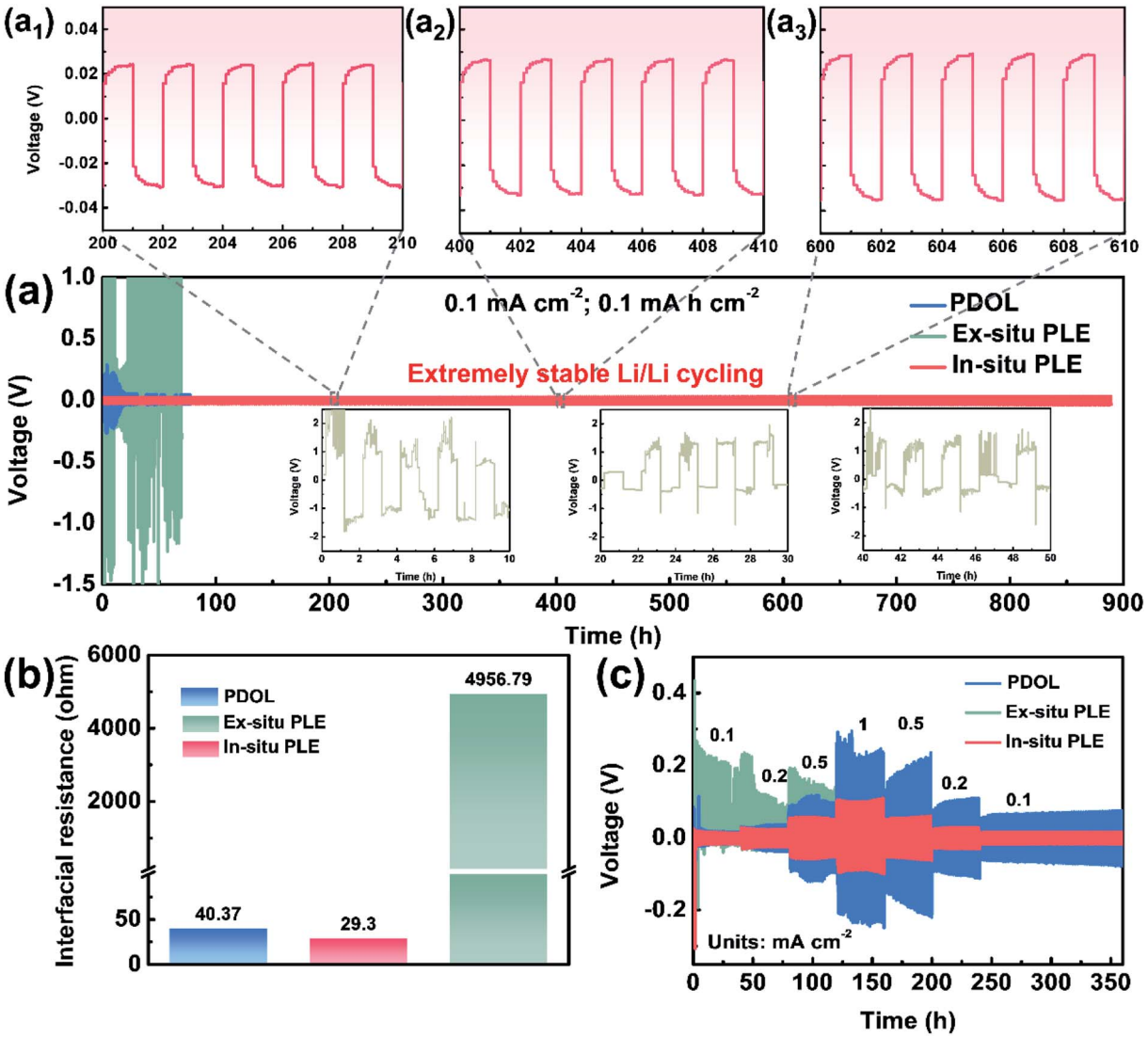

Fig. 3 Electrochemical characterization of different composite polymer electrolytes: (a) long-term cycling stabilities of symmetric cell; (a_1–a_3) enlarged voltage–time curves with periods of 200–210, 400–410 and 600–610 h. (b) Interfacial resistance (R_{ct}) analyses before cycling. (c) Rate capabilities of Li|Li symmetrical cells.

from rigid ion transport at the solid–solid interface would lead to large amounts of dead lithium and rapid cell failure. Meanwhile, the Li|PDOL|Li cell with low R_{ct} can maintain normal circulation but is hindered by the poor mechanical properties of the PDOL electrolyte. On the contrary, the Li|*In-situ* PLE|Li cell presents a very low initial R_{ct} of only 29.3 Ω and remains stable without any obvious increase after 300th cycling, which is consistent with the Li-plating/stripping curves.

Aside from interfacial wettability and conductivity, symmetric batteries were also conducted to evaluate the Li^+ transmission rate (Fig. 3c). By constantly changing the current density to different values (0.1, 0.2, 0.5, 1, 0.5, 0.2 to 0.1 mA cm^{-2}), the *In-situ* PLE symmetric cell shows the lowest polarization voltages of 40, 60, 92, 182, 110, 56 and 32 mV, respectively. The overpotential of *In-situ* PLE presents some fluctuations in the first 3 h, probably because of the formation of SEI. Even under high variation rates, it maintains stable cycling without polarization or short circuit phenomena. In contrast, the Li|*Ex-situ* PLE|Li cell exhibits an asymmetrical electrochemical curve due to its high interfacial transport barrier (Fig. 3b) and lithium dendrites form inside the *Ex-situ* PLE skeleton when the potential reaches <0 V *versus* Li/Li^+.[30] This is directly supported by the X-ray photoelectron spectroscopy (XPS) analyses in Fig. S11.† Compared with the white LLTO NFs in the Li|*In-situ* PLE|Li cell, the LLTO NFs in the Li|*Ex-situ* PLE|Li cell present the black color with the existence of oxygen vacancies (Fig. S11a–c†). The appearance of peaks corresponding to Ti^{3+} further prove the electrochemical instability of the *Ex-situ* PLE (Fig. S11d†).[30]

To elucidate the reasons behind long-cycle stability, the surface features and chemical compositions of the Li anode were evaluated by *ex situ* SEM and XPS measurements after cycling. Fig. 4a–f presents the top-view SEM images of the cycled Li electrode at low and high magnifications. Evidently, there are

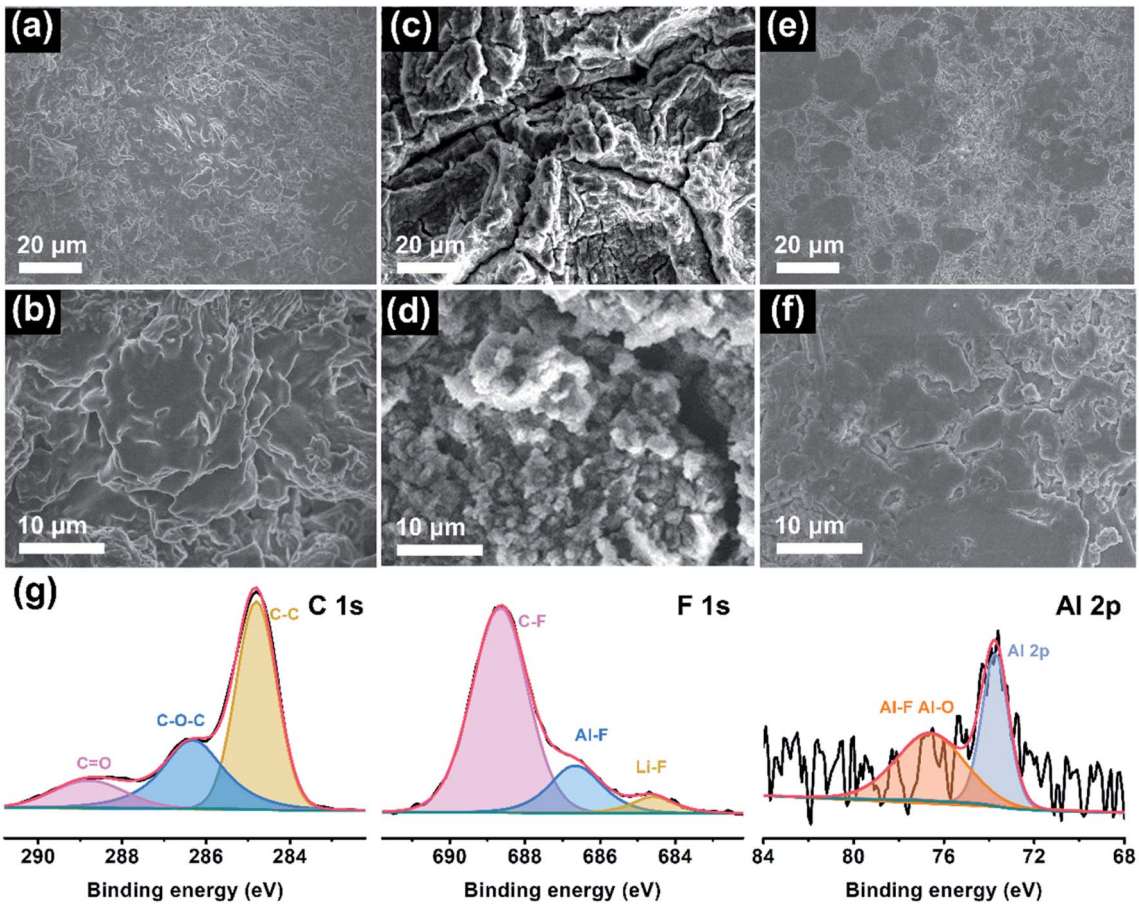

Fig. 4 Interfacial characterizations of the anode surface. SEM images of Li metal after 50 cycles with (a and b) PDOL electrolyte, (c and d) *Ex-situ* PLE and (e and f) *In-situ* PLE. (g) XPS spectra of the cycled Li anode from the symmetric battery using *In-situ* PLE.

many chaotic clusters unevenly distributed on the anode surface in the PDOL-based battery (Fig. 4a and b). These bulk and loose Li clusters will evolve into dendrites in subsequent cycles, which is deemed to be the foremost reason for the sudden short circuit of the corresponding cell at 80 h, as shown in Fig. 3a. Further, the *Ex-situ* PLE symmetric cell displays a rugged Li surface with lots of scratches and cracks, and metallic particles appear at higher magnification (Fig. 4c and d). The harsh structural failure indicates the disordered Li electrodeposition behavior on the Li anode, which reveals unstable Li plating/stripping kinetics. In sharp contrast, the anode surface in the Li|*In-situ* PLE|Li cell after cycling is flat and dense without obvious defects (Fig. 4e and f), which contributes to the sturdy mechanical and sustainable chemical behaviors of the composite polyether electrolyte, and ensures the long circulation of the symmetric cell. Moreover, XPS analysis further investigates the chemical state of the SEI on the Li metal anode in *In-situ* PLE. As shown in Fig. 4g, the main peaks of the C 1s spectrum come from the polymer chain. Due to the electrochemical decomposition of $N(CF_3SO_2)^{2-}$ ($TFSI^-$) anions on the anode surface, an obvious signal of LiF is detected, implying that a LiF-rich SEI film is formed, which is known as an electric insulator with a low activation energy barrier for Li diffusion to stabilize the electrode/electrolyte interface.[35–38] Simultaneously, an Al signal from residual $Al(OTf)_3$ is also detected (Fig. S12†). The Al–F and Al–O species generated from the $Al(OTf)_3$ decomposition participate in the construction of SEI, in which the aluminum complex (AlF_3 and Al_2O_3) contribute to the reduced energy of lithium salt dissociation and act as an anodic protective film, respectively. It is also beneficial for the formation of a stable and robust SEI, thus enhancing the stability of the Li metal anode.[29,39,40] The above results confirm the excellent effects of the *In-situ* PLE in interfacial passivation and the inhibition of dendrite growth.

Inspired by the high oxidation features of the designed *In-situ* PLE, full batteries composed of $LiFePO_4$ (LFP) cathode and solid electrolytes were further evaluated to assess its practical compatibility (Fig. 5a). The Li|PDOL|LFP full battery exhibits a huge capacity fluctuation in the first 25 cycles, and a steep drop from 121.6 to 92.9 mA h g^{-1} along with high polarization voltage after 95 cycles (Fig. S13†). Similarly, the Li|*Ex-situ* PLE|LFP delivers an initial discharge capacity of 118.8 mA h g^{-1} and drops to 69.4 mA h g^{-1} with unsatisfactory retention of only 57.6% after 120 cycles. Surprisingly, the Li|*In-situ* PLE|LFP full battery achieves an enhanced specific capacity of 157.6 mA h g^{-1} and can still reach up to 70.7% after 350 cycles with an average CE of 99.9%. Fig. 5b shows the rate stability from 0.1C to 2C, where the PDOL-assembled battery is reduced

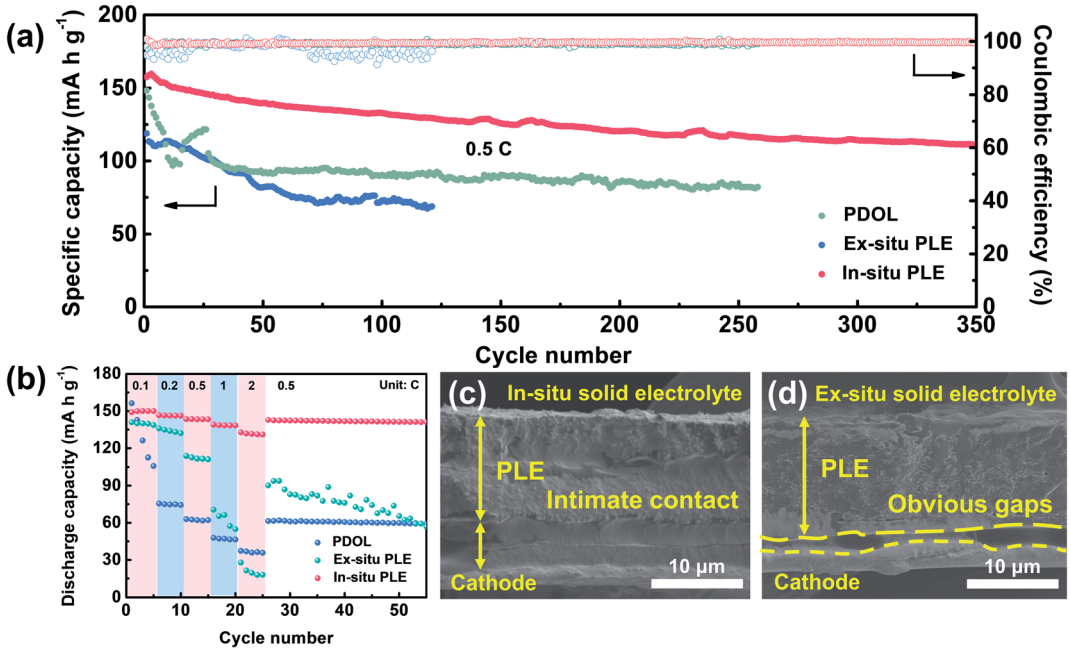

Fig. 5 (a) The long-term cycling stability of Li|LFP full batteries at 0.5C. (b) The rate capability of full batteries with different electrolytes. Cross-sectional views of the cycled Li|$LiFePO_4$ batteries assembled with (c) *In-situ* PLE, and (d) *Ex-situ* PLE.

from 156.3 to 105.8 mA h g^{-1} after 5 cycles, and finally reaches 59.2 mA h g^{-1} when recovered to 0.5C. This can be traced to the inherent weak mechanical resistance and low conductivity of the PDOL. The battery assembled with *Ex-situ* PLE also presents inferior capacity maintenance under various current rates. Most notably, the Li|*In-situ* PLE|LFP full battery delivers high discharge capacities of 149, 146.6, 143.5, 139 and 132.8 mA h g^{-1} at 0.1, 0.2, 0.5, 1 and 2C, respectively. It is worth mentioning that when the current rate is recovered to 0.5C, the capacity remains at 142.5 mA h g^{-1}, further indicating the superior reversible rate capability. This can be ascribed to the excellent interfacial ion transport and high bulk ion conduction of the *In-situ* PLE assembled battery, with a continuous interface between the *In-situ* PLE and LFP cathode compared to the clear gaps between the *Ex-situ* PLE and LFP cathode (Fig. 5c and d).

Conclusions

In summary, a topochemistry-driven polyether electrolyte is incorporated into the 3D fast ion conductor of LLTO NF skeleton *via in situ* polymerization, which synergistically addresses the chemical/electrochemical interfacial instability, low ionic conductivity, and poor cyclability of solid lithium metal batteries. The unique amorphous structure of CH_2–CH_2–O–CH_2–O– in PDOL effectively promotes bulk and interfacial ion transfer, contributing to a wide window of 5.5 V and t_{Li}^{+} of 0.6. Moreover, the generated LiF and Al-complex film can also hinder dendrite growth and the formation of dead Li. Arising from bi-phase transport paths, the polyether-based composite electrolyte exhibits a comparatively high σ of 6.6×10^{-4} S cm^{-1}. Therefore, the Li metal anode with *In-situ* PLE can stably work at high rates for over 900 h without dendrite growth. The assembled LMBs with LFP cathode show a high capacity retention of 70.7% after 350 cycles at 0.5C, with a satisfactory coulombic efficiency of 99.9%.

Conflicts of interest

There are no conflicts to declare.

Acknowledgements

This project was funded by the National Natural Science Foundation of China (22075042), Shanghai Rising-Star Program (22QA1400300), the Natural Science Foundation of Shanghai (20ZR1401400), the Fundamental Research Funds for the Central Universities and the DHU Distinguished Young Professor Program (LZB2021002).

Notes and references

1 K. J. Kim, M. Balaish, M. Wadaguchi, L. Kong and J. L. M. Rupp, *Adv. Energy Mater.*, 2021, **11**, 2002689.
2 C. Ma, C. Liu, Y. Zhang, X. Zhang, Z. Zhao, T. Song, B. Wu and D. Mu, *Chem. Eng. J.*, 2022, **434**, 134637.
3 G. Li, *Adv. Energy Mater.*, 2021, **11**, 2002891.
4 F. Shi, C. Chen and Z. L. Xu, *Adv. Fiber Mater.*, 2021, **3**, 275–301.
5 X. R. Chen, B. C. Zhao, C. Yan and Q. Zhang, *Adv. Mater.*, 2021, **33**, 2004128.
6 Y. Y. Chen, G. Y. Zhou, W. Zong, Y. Ouyang, K. Chen, Y. Lv, Y. E. Miao and T. X. Liu, *Compos. Commun.*, 2021, **25**, 100679.
7 H. J. Kim, N. Umirov, J. S. Park, J. H. Lim, J. Zhu, S. S. Kim and S. T. Myung, *Energy Storage Mater.*, 2022, **46**, 76–89.

8 C. Y. Zhou, W. Zong, G. Y. Zhou, X. S. Fan and Y. E. Miao, *Compos. Commun.*, 2021, **25**, 100696.
9 Y. Ren and K. B. Hatzell, *J. Mater. Chem. A*, 2021, **9**, 13804–13821.
10 P. Ding, Z. Lin, X. Guo, L. Wu, Y. Wang, H. Guo, L. Li and H. Yu, *Mater. Today*, 2021, **51**, 449–474.
11 C. Zhao, X. Yao, H. Yang, X. Jiao and L. Wang, *Compos. Commun.*, 2021, **26**, 100789.
12 K. Jiang, J. Wang, C. Zuo, S. Li, S. Li, D. He, H. Peng, X. Xie, R. Poli and Z. Xue, *Macromolecules*, 2020, **53**, 7450–7459.
13 K. Zhang, F. Wu, X. Wang, L. Zheng, X. Yang, H. Zhao, Y. Sun, W. Zhao, Y. Bai and C. Wu, *Adv. Funct. Mater.*, 2022, 2107764.
14 H. He, Y. Chai, X. Zhang, P. Shi, J. Fan, Q. Xu and Y. Min, *J. Mater. Chem. A*, 2021, **9**, 9214–9227.
15 J. Zhang, X. Zang, H. Wen, T. Dong, J. Chai, Y. Li, B. Chen, J. Zhao, S. Dong, J. Ma, L. Yue, Z. Liu, X. Guo, G. Cui and L. Chen, *J. Mater. Chem. A*, 2017, **5**, 4940–4948.
16 T. Dong, J. Zhang, G. Xu, J. Chai, H. Du, L. Wang, H. Wen, X. Zang, A. Du, Q. Jia, X. Zhou and G. Cui, *Energy Environ. Sci.*, 2018, **11**, 1197–1203.
17 Q. Wang, T. Dong, Q. Zhou, Z. Cui, X. Shangguan, C. Lu, Z. Lv, K. Chen, L. Huang, H. Zhang and G. Cui, *Sci. China Chem.*, 2022, **65**, 934–942.
18 Z. Geng, Y. Huang, G. Sun, R. Chen, W. Cao, J. Zheng and H. Li, *Nano Energy*, 2021, **91**, 106679.
19 Z. Shen, Y. Cheng, S. Sun, X. Ke, L. Liu and Z. Shi, *Carbon Energy*, 2021, **3**, 482–508.
20 J. Pan, H. Peng, Y. Yan, Y. Bai, J. Yang, N. Wang, S. Dou and F. Huang, *Energy Storage Mater.*, 2021, **43**, 165–171.
21 Y. Yan, J. Ju, S. Dong, Y. Wang, L. Huang, L. Cui, F. Jiang, Q. Wang, Y. Zhang and G. Cui, *Adv. Sci.*, 2021, **8**, 2003887.
22 Y. Liu, H. Su, M. Li, J. Xiang, X. Wu, Y. Zhong, X. Wang, X. Xia, C. Gu and J. Tu, *J. Mater. Chem. A*, 2021, **9**, 13531–13539.
23 J. Bae, Y. Li, J. Zhang, X. Zhou, F. Zhao, Y. Shi, J. B. Goodenough and G. Yu, *Angew. Chem., Int. Ed.*, 2018, **57**, 2096–2100.
24 Y. Wang, J. Ju, S. Dong, Y. Yan, F. Jiang, L. Cui, Q. Wang, X. Han and G. Cui, *Adv. Funct. Mater.*, 2021, **31**, 2101523.
25 R. Lv, W. Kou, S. Guo, W. Wu, Y. Zhang, Y. Wang and J. Wang, *Angew. Chem., Int. Ed.*, 2022, **61**, 202114220.
26 Q. Zhao, X. Liu, S. Stalin, K. Khan and L. A. Archer, *Nat. Energy*, 2019, **4**, 365–373.
27 C. Liu, F. Zhu, Z. Huang, W. Liao, X. Guan, Y. Li, D. Chen and Z. Lu, *Chem. Eng. J.*, 2022, **434**, 134644.
28 Q. Zhang, X. Liu, H. Li, Z. Guo, T. Bian, X. Zhu, N. Zhan and Y. Zhao, *Small*, 2022, 2106395.
29 Y. Liu and Y. Xu, *Chem. Eng. J.*, 2022, **433**, 134471.
30 S. Liu, Y. Zhao, X. Li, J. Yu, J. Yan and B. Ding, *Adv. Mater.*, 2021, **33**, 2008084.
31 Y. He, N. Liu and P. A. Kohl, *J. Electrochem. Soc.*, 2020, **167**, 100517.
32 W. P. Chen, H. Duan, J. L. Shi, Y. Qian, J. Wan, X. D. Zhang, H. Sheng, B. Guan, R. Wen, Y. X. Yin, S. Xin, Y. G. Guo and L. J. Wan, *J. Am. Chem. Soc.*, 2021, **143**, 5717–5726.
33 H. Huo, Y. Chen, J. Luo, X. Yang, X. Guo and X. Sun, *Adv. Energy Mater.*, 2019, **9**, 1804004.
34 F. He, W. Tang, X. Zhang, L. Deng and J. Luo, *Adv. Mater.*, 2021, **33**, 2105329.
35 A. Hu, W. Chen, X. Du, Y. Hu, T. Lei, H. Wang, L. Xue, Y. Li, H. Sun, Y. Yan, J. Long, C. Shu, J. Zhu, B. Li, X. Wang and J. Xiong, *Energy Environ. Sci.*, 2021, **14**, 4115–4124.
36 O. Sheng, J. Zheng, Z. Ju, C. Jin, Y. Wang, M. Chen, J. Nai, T. Liu, W. Zhang, Y. Liu and X. Tao, *Adv. Mater.*, 2020, **32**, 2000223.
37 O. Sheng, C. Jin, X. Ding, T. Liu, Y. Wan, Y. Liu, J. Nai, Y. Wang, C. Liu and X. Tao, *Adv. Funct. Mater.*, 2021, **31**, 2100891.
38 M. Chen, J. Zheng, Y. Liu, O. Sheng, Z. Ju, G. Lu, T. Liu, Y. Wang, J. Nai, Q. Wang and X. Tao, *Adv. Funct. Mater.*, 2021, **31**, 2102228.
39 Y. He, Y. Zhang, Z. Wang, X. Li, Z. Lü, X. Huang and Z. Liu, *Adv. Funct. Mater.*, 2021, **31**, 2101737.
40 X. Zhang, J. Xie, F. Shi, D. Lin, Y. Liu, W. Liu, A. Pei, Y. Gong, H. Wang, K. Liu, Y. Xiang and Y. Cui, *Nano Lett.*, 2018, **18**, 3829–3838.

